

PROBE: Probabilistic Occupancy BEV Encoding with Analytical Translation Robustness for 3D Place Recognition

Jinseop Lee¹, ByoungHo Lee², and Gichul Yoo^{3*}

Abstract—We present PROBE (PRobabilistic Occupancy BEV Encoding), a learning-free LiDAR place recognition descriptor that models each BEV cell’s occupancy as a Bernoulli random variable. Rather than relying on discrete point-cloud perturbations, PROBE analytically marginalizes over continuous Cartesian translations via the polar Jacobian, yielding a distance-adaptive angular uncertainty $\sigma_\theta = \sigma_t/r$ in $O(R \times S)$ time. The primary parameter σ_t represents the expected translational uncertainty in meters, a sensor-independent physical quantity allowing cross-sensor generalization without per-dataset tuning. Pairwise similarity combines a *Bernoulli-KL Jaccard* with exponential uncertainty gating and FFT-based height cosine similarity for rotation alignment. Evaluated on four datasets spanning four diverse LiDAR types, PROBE achieves the highest accuracy among handcrafted descriptors in multi-session evaluation and competitive single-session performance against both handcrafted and supervised baselines. The source code and supplementary materials are available at <https://sites.google.com/view/probe-pr>.

Index Terms—LiDAR, Bird’s-Eye View, Place Recognition, Global Localization, Loop Closure Detection.

I. INTRODUCTION

PLACE recognition, the ability to re-identify previously visited locations from sensor observations, is a critical component of simultaneous localization and mapping (SLAM) [1], enabling loop closure detection, kidnapped-robot recovery, and multi-session map merging. Among the various sensor modalities, 3D LiDAR is widely adopted due to its illumination invariance and accurate range measurements.

Existing LiDAR place recognition methods can be broadly categorized into three families. *Handcrafted global descriptors* project each scan into a compact representation, typically a Bird’s-Eye-View (BEV) polar grid [2]–[5] or range-elevation bins [6], and resolve the heading ambiguity via exhaustive circular shift or frequency-domain matching. These methods are lightweight and require no training. *Learning-based methods* [7]–[10] extract global features via deep networks, achieving strong generalization at the cost of GPU inference and training data. *Local feature methods* [11], [12] detect keypoints and build geometric constraints for verification, but require additional geometric verification stages and are less suited to standalone pairwise evaluation.

*Corresponding author.

J. Lee, B. Lee, and G. Yoo are with the AX Tech, SK Intel-lig, Seoul, Republic of Korea (e-mail: jinseop.lee@gmail.com, byoungHo.lee@sk.com, gichul.yoo@sk.com).

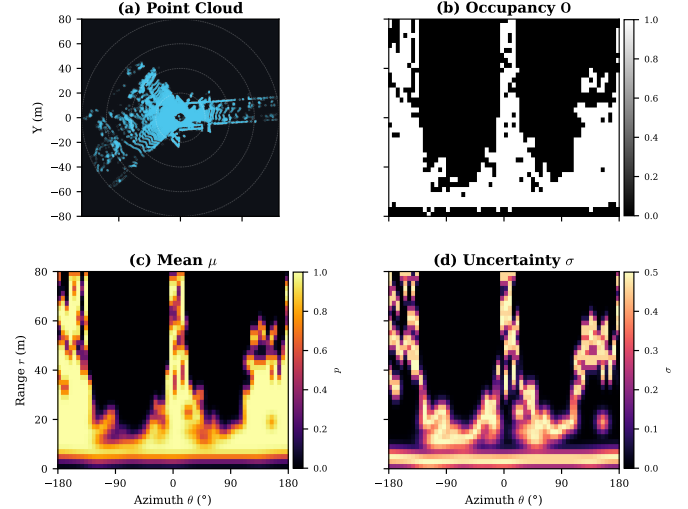


Fig. 1: PROBE encodes a LiDAR point cloud (top-left) into a probabilistic polar BEV grid. The binary occupancy mask O (top-right), Bernoulli mean μ (bottom-left), and per-cell uncertainty σ (bottom-right) are computed via Jacobian-derived analytical marginalization. High- σ boundary cells are automatically downweighted during matching.

Despite their practical success, the handcrafted BEV family, to which PROBE belongs, suffers from a fundamental limitation that remains an open challenge.

Binary occupancy and heuristic translation invariance. BEV polar grids are inherently sensitive to translational shifts: a small lateral displacement of the sensor origin can toggle boundary cells between occupied and empty, corrupting the matching score. SC++ [3] mitigates this by constructing descriptors at a small number of laterally shifted grid origins, but covering only a discrete set of offsets leaves residual sensitivity to arbitrary displacements. Binary occupancy matching further exacerbates this issue by treating all mismatched cells equally, without distinguishing geometrically stable cells from volatile boundary cells that toggle under slight viewpoint changes.

We propose **PROBE (PRobabilistic Occupancy BEV Encoding)**, which replaces heuristic binary matching with a probabilistic model. Instead of discrete spatial sampling, PROBE projects isotropic Cartesian translation uncertainty into the polar domain via the Jacobian. This *analytical marginalization* models each cell as a Bernoulli random variable (μ, σ) within a single BEV grid (Fig. 1), where

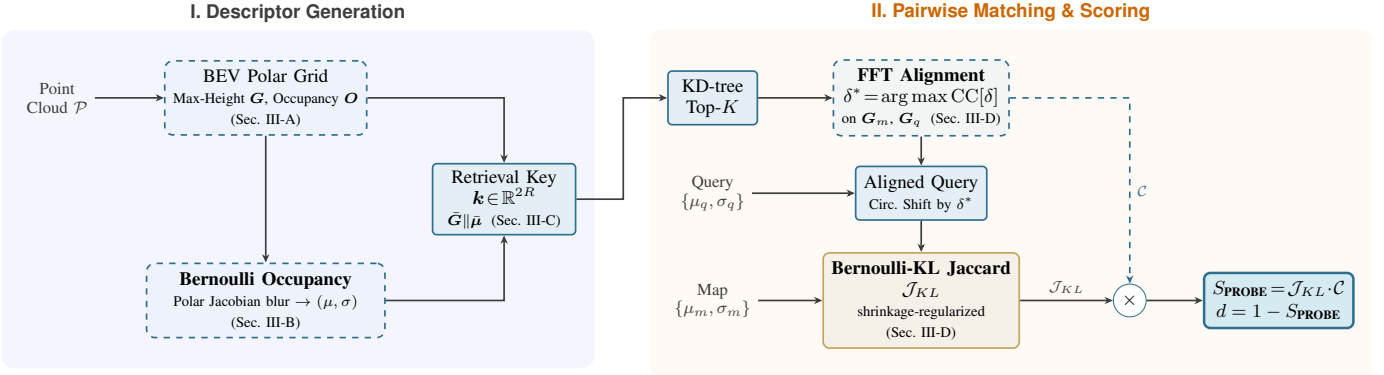


Fig. 2: PROBE pipeline. **(I)** Descriptor generation: a BEV polar grid \mathbf{G} is built with max-height encoding and occupancy mask \mathbf{O} . Analytical marginalization via the polar Jacobian produces per-cell Bernoulli occupancy (μ, σ) . A rotation-invariant ring-mean key $\mathbf{k} \in \mathbb{R}^{2R}$ is formed for KD-tree pre-filtering. **(II)** Pairwise scoring: FFT-based rotation alignment on the max-height grids yields δ^* ; the query is circularly shifted to produce an aligned query, which is scored against the map via a shrinkage-regularized Bernoulli-KL Jaccard \mathcal{J}_{KL} . The final score fuses \mathcal{J}_{KL} with the height cosine similarity $\mathcal{C} = \text{CC}[\delta^*]$ multiplicatively: $S_{\text{PROBE}} = \mathcal{J}_{KL} \cdot \mathcal{C}$.

the distance-adaptive uncertainty $\sigma_\theta = \sigma_t/r$ follows directly from the polar coordinate transform. PROBE then employs a *Bernoulli-KL Jaccard* that downweights uncertain cells through exponential gating, combined with FFT-accelerated cosine similarity for rotation alignment.

The main contributions are:

- 1) **Analytical Marginalization via Polar Jacobian:** We replace computationally expensive discrete point-cloud perturbations with a closed-form probabilistic model. By applying a Jacobian-derived adaptive 1D spatial blur, we analytically marginalize continuous Cartesian translations into a single BEV grid in $O(R \times S)$ time, yielding a distance-adaptive angular uncertainty ($\sigma_\theta = \sigma_t/r$) and eliminating the need for generating multiple virtual views.
- 2) **Bernoulli-KL Jaccard with Uncertainty Gating:** a pairwise scoring mechanism that smooths each cell’s occupancy toward an uninformative prior proportionally to its uncertainty, computes symmetric KL divergence, and downweights high- σ cells via exponential gating. This replaces the standard binary Jaccard with a divergence measure that distinguishes stable structures from viewpoint-sensitive boundaries.
- 3) **Cross-sensor generalization with a single physically-grounded parameter:** the primary parameter σ_t represents the expected translational uncertainty in meters, a sensor-independent physical quantity that generalizes to unseen sensors and environments without per-dataset tuning, as validated across 22 sequence configurations spanning four LiDAR types (KITTI, HeLiPR, NCLT, ComplexUrban).

II. RELATED WORK

A. Handcrafted Global Descriptors

The BEV polar grid is a standard representation for lightweight LiDAR place recognition. M2DP [13] projects the

cloud onto multiple 2-D planes at varying azimuths and elevations and applies SVD to produce a compact global descriptor that aims for rotation invariance, though its fixed projection geometry limits adaptability to varying sensor configurations. Scan Context (SC) [2] projects each scan into an $R \times S$ grid of maximum heights and aligns two descriptors by exhaustively shifting columns, selecting the azimuth with the lowest cosine distance. LiDAR-Iris [4] applies a Fourier transform to achieve rotation invariance, and binarizes features extracted via LoG-Gabor filtering for fast Hamming-distance matching. SC++ [3] accelerates retrieval via ring and sector keys and introduces a Cartesian Context that discretizes the BEV on a Cartesian grid, enabling linear-shift alignment that is more robust to translational offset. RING++ [5] applies Radon and Fourier transforms to multi-channel BEV features, producing roto-translation invariant descriptors. SOLiD [6] reweights range-elevation bins to handle restricted field-of-view scenarios on heterogeneous platforms.

Among the above descriptors, most do not explicitly address translational offset. SC++ [3] is a notable exception, synthesizing laterally shifted copies of the descriptor to cover plausible displacements, though at increased matching cost. RING++ [5] achieves roto-translation invariance through spectral transforms, yet its strong invariance can match geometrically similar but spatially distant places, reducing recognition precision. PROBE addresses these limitations by replacing heuristics with analytical marginalization over continuous translations, encoding per-cell Bernoulli occupancy and uncertainty within a single grid to downweight uncertain cells.

B. Learning-Based Descriptors

PointNetVLAD [7] aggregates PointNet features with a NetVLAD layer for metric retrieval from raw point clouds. OverlapNet [8] estimates pairwise overlap and yaw offset from range images. MinkLoc3D [10] applies sparse 3D convolutions to voxelized point clouds, achieving strong recall with a compact descriptor. LoGG3D-Net [14] combines local

consistency loss with a global descriptor head for geometry-aware retrieval. OverlapTransformer [9] augments a convolutional range-image encoder with a lightweight transformer to achieve yaw-angle invariance with sub-2-ms inference. BEV-Place++ [15] renders point clouds into BEV images and trains a rotation-equivariant CNN-NetVLAD pipeline to produce compact global descriptors with fast nearest-neighbor retrieval. These methods generalize well but depend on training data and GPU inference, which limits their use on embedded platforms. PROBE achieves comparable accuracy through probabilistic modeling without any learned parameters.

C. Local Feature Methods

BTC [11] extracts keypoints from detected planes, forms triangles as viewpoint-invariant global descriptors, and verifies matches via point correspondence. STD [12] extracts stable triangles from keypoints for loop closure detection within SLAM pipelines. While these approaches perform well when integrated with a mapping backend, their reliance on explicit geometric verification restricts inference speed, making them less suited for standalone pairwise evaluation.

D. Positioning of PROBE

PROBE belongs to the handcrafted BEV family but replaces deterministic binary matching with probabilistic occupancy modeling: (i) *analytical marginalization* via the polar Jacobian produces a per-cell Bernoulli model in closed form; (ii) a *Bernoulli-KL Jaccard with uncertainty gating* replaces the binary Jaccard with a divergence measure that downweights unreliable cells. Like SC and SC++, PROBE requires no training and no geometric verification, yet achieves accuracy competitive with learning-based methods. For a comprehensive review of LiDAR-based place recognition methods, we refer the reader to [16]. To our knowledge, no existing method models per-cell occupancy as a Bernoulli random variable with analytically derived uncertainty for BEV-based place recognition.

III. METHODOLOGY

Given a 3D LiDAR point cloud $\mathcal{P} = \{(x_i, y_i, z_i)\}_{i=1}^N$, PROBE constructs a compact descriptor and scores pairwise similarity in four steps (Fig. 2): (i) BEV polar grid construction with max-height encoding, (ii) per-cell Bernoulli occupancy estimation via Jacobian-derived analytical marginalization, (iii) ring-mean retrieval key for KD-tree pre-filtering, and (iv) FFT-based rotation alignment with Bernoulli-KL Jaccard scoring.

A. BEV Grid Construction

Following the Scan Context framework [2], each point is projected into a polar BEV grid $\mathbf{G} \in \mathbb{R}^{R \times S}$, where R rings partition the horizontal range $[0, R_{\max}]$ and S sectors partition the azimuth $[0, 2\pi)$. Each cell stores the maximum height of its constituent points; empty cells are zero. A binary occupancy mask

$$\mathbf{O}[r, s] = \begin{cases} 1 & \text{if cell } (r, s) \text{ contains } \geq 1 \text{ point,} \\ 0 & \text{otherwise,} \end{cases} \quad (1)$$

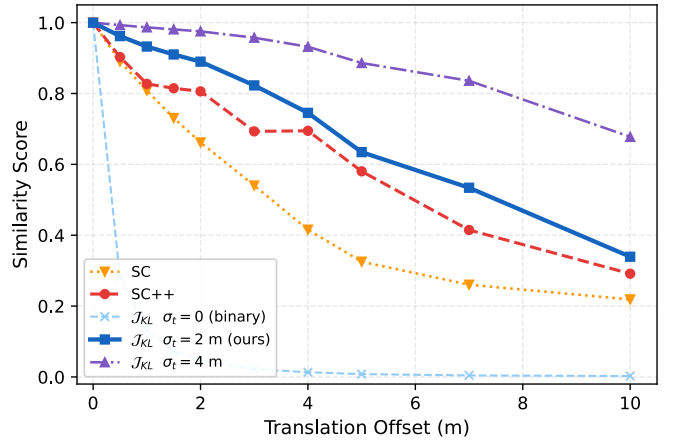


Fig. 3: Translation robustness: similarity under increasing lateral translation on KITTI-08 (averaged over 7 frames and 3 translation directions). SC (no augmentation) degrades fastest; SC++ mitigates this via discrete augmentation, producing a characteristic plateau. The Bernoulli-KL Jaccard \mathcal{J}_{KL} is shown at three blur levels: without blur ($\sigma_t=0$, dashed), $\sigma_t=2$ m (proposed), and $\sigma_t=4$ m. Analytical marginalization transforms a brittle binary descriptor into a smoothly robust one.

records whether each cell is occupied.

B. Per-Cell Bernoulli Occupancy Model

A key limitation of binary occupancy matching is that boundary cells—those at the edge of observable structures—are unstable: a small translational offset of the sensor origin can toggle their occupancy state. Rather than treating all cells equally, PROBE models each cell as a Bernoulli random variable $\text{Bernoulli}(\mu)$ and estimates a per-cell uncertainty σ by analytically marginalizing over continuous translations using the polar-grid Jacobian. Both quantities are then exploited for adaptive scoring in Section III-D.

Jacobian-derived adaptive blur. Consider a point at polar coordinates (r_0, θ_0) . An isotropic Cartesian translation $\Delta \mathbf{x} = (\Delta x, \Delta y)^T \sim \mathcal{N}(\mathbf{0}, \sigma_t^2 \mathbf{I})$ induces polar perturbations via the Jacobian matrix $\mathbf{J} = \partial(r, \theta) / \partial(x, y)$. The propagated polar covariance, obtained via a first-order Taylor approximation, is

$$\Sigma_{\text{polar}} \approx \mathbf{J}(\sigma_t^2 \mathbf{I}) \mathbf{J}^T = \begin{bmatrix} \sigma_t^2 & 0 \\ 0 & \sigma_t^2 / r_0^2 \end{bmatrix}. \quad (2)$$

This yields the following decoupled perturbation distributions:

$$\Delta r \sim \mathcal{N}(0, \sigma_t^2), \quad \Delta \theta \sim \mathcal{N}(0, \sigma_t^2 / r_0^2). \quad (3)$$

The angular uncertainty decreases with range: nearby cells are more sensitive to lateral translation than distant ones, yielding the characteristic $\sigma_\theta \propto 1/r$ relationship. This first-order approximation is accurate when $\sigma_t \ll r_0$, which holds for all practical ring indices beyond the first few meters.

Proposition 1 (Translation Marginalization). Let $\mathbf{O}[r, s] \in \{0, 1\}$ be the binary occupancy of the polar grid. The expected

occupancy under isotropic Cartesian translation uncertainty $\Delta\mathbf{x} \sim \mathcal{N}(\mathbf{0}, \sigma_t^2 \mathbf{I})$ is

$$\mu[r, s] = \mathbb{E}_{\Delta\mathbf{x}}[\mathbf{O}[r+\Delta r, s+\Delta\theta]] = (\mathbf{O} * \mathcal{G}_{\text{polar}})[r, s], \quad (4)$$

where $\mathcal{G}_{\text{polar}}$ is a separable Gaussian kernel with widths σ_r and $\sigma_\theta(r)$ given by (3).

Proof sketch. Since \mathbf{O} is binary, $\mathbb{E}[\mathbf{O}]$ reduces to the probability that the randomly perturbed cell falls in an occupied region. By (2), the Cartesian perturbations map to locally decorrelated Gaussian noise in the polar domain ($\Delta r \perp \Delta\theta$). Thus, the 2-D expectation factorizes into two sequential 1-D convolutions, enabling efficient separable filtering directly on the polar grid:

$$\text{Step 1: } \mu[r, \cdot] \leftarrow G_{1\text{D}}(\mathbf{O}[r, \cdot]; \sigma_\theta(r), \text{wrap}), \quad (5)$$

$$\text{Step 2: } \mu[\cdot, s] \leftarrow G_{1\text{D}}(\mu[\cdot, s]; \sigma_r, \text{constant}), \quad (6)$$

where $G_{1\text{D}}(\cdot; \sigma, \text{mode})$ denotes 1-D Gaussian convolution with boundary handling, $\sigma_\theta(r) = \sigma_{\text{eff}}(r)/(r_{\text{center}} \cdot \Delta\theta)$ is the angular kernel width in sector-cell units, and $\sigma_r = \sigma_t/\Delta r$ is the radial kernel width in ring-cell units, with $\Delta\theta = 2\pi/S$ and $\Delta r = R_{\text{max}}/R$ being the grid resolutions. The resulting $\mu[r, s] \in [0, 1]$ is exactly the marginal occupancy probability under the assumed translation model. \square

Density-adaptive σ_{eff} . The Gaussian kernel assumes a continuous occupancy field; however, LiDAR provides discrete samples whose density varies with range and sensor resolution. For the angular blur (5), we scale the effective kernel bandwidth by the local occupancy density:

$$\sigma_{\text{eff}}(r) = \sigma_t \cdot \sqrt{\rho(r)}, \quad (7)$$

where $\rho(r) = \frac{1}{S} \sum_s \mathbf{O}[r, s]$ is the per-ring occupancy rate. The $\sqrt{\rho}$ factor scales the blur proportionally to the observed density, preventing overconfident smoothing when few cells are populated. Dense rings ($\rho \approx 1$) receive full blur, preserving the theoretical uncertainty model. Sparse rings ($\rho \ll 1$) receive reduced blur, preventing over-smoothing that would obscure local structures. The radial blur (6) uses the theoretical constant $\sigma_r = \sigma_t/\Delta r$ uniformly, since the Jacobian-derived radial uncertainty (3) is independent of position.

The per-cell Bernoulli uncertainty σ is then derived directly from the blurred occupancy μ . Since the original mask \mathbf{O} is binary ($\mathbf{O}^2 = \mathbf{O}$), the variance simplifies to:

$$\sigma[r, s] = \sqrt{\mu[r, s] - (\mu[r, s])^2} = \sqrt{\mu[r, s](1 - \mu[r, s])}, \quad (8)$$

attaining a maximum of $\sigma = 0.5$ for maximally uncertain cells ($\mu = 0.5$) and vanishing for confident cells ($\mu \approx 0$ or $\mu \approx 1$).

Interpretation. Cells deep within a structure’s footprint retain $\mu \approx 1$ after blurring, yielding $\sigma \approx 0$: the blur merely reinforces the occupied region. Boundary cells where the blur spreads occupancy across the occupied/empty edge produce intermediate μ and correspondingly high σ , signaling low confidence. The density-adaptive scaling ensures that this mechanism scales down on sparse sensors (e.g., 32-beam LiDAR) by reducing blur where the sampling density is insufficient to support the assumed convolution. Fig. 3 illustrates the resulting translation robustness.

TABLE I: Computational Complexity Comparison. N : points, R : rings, S : sectors, H : height bins, K : column search window ($K \leq S$).

Method	Construction	Per-Pair Matching
SC [2]	$\mathcal{O}(N)$	$\mathcal{O}(K \cdot R \cdot S)$
SC++ [3]	$\mathcal{O}(K' \cdot N)$	$\mathcal{O}(K \cdot R \cdot S)$
SOLiD [6]	$\mathcal{O}(N + R \cdot H)$	$\mathcal{O}(R)$
PROBE (Ours)	$\mathcal{O}(N + R \cdot S \log S)$	$\mathcal{O}(R \cdot S + S \log S)$

C. Ring-Mean Retrieval Key

For large-scale place recognition, exhaustive pairwise scoring is prohibitive. Following the ring-key paradigm of SC [2], PROBE constructs a compact *retrieval key* per descriptor for KD-tree nearest-neighbor pre-filtering. A key design requirement is *rotation invariance*: the key must be identical regardless of the sensor heading, since the full rotation search is deferred to the pairwise scoring stage.

Row-wise mean as rotation-invariant feature. Since the azimuthal sum (or mean) over all sectors in a ring is invariant to circular shifts, each ring’s mean provides a rotation-invariant scalar. PROBE concatenates two complementary ring-mean vectors:

$$\mathbf{k} = [\bar{\mathbf{G}} \parallel \bar{\boldsymbol{\mu}}] \in \mathbb{R}^{2R}, \quad (9)$$

where $\bar{\mathbf{G}}[r] = \frac{1}{S} \sum_s \mathbf{G}[r, s]$ captures the *expected height profile* across rings (vertical geometry), and $\bar{\boldsymbol{\mu}}[r] = \frac{1}{S} \sum_s \boldsymbol{\mu}[r, s]$ captures the *marginal occupancy probability* (planar density). The latter inherits translation robustness from the analytical marginalization.

The resulting $2R$ -dimensional key is compact yet discriminative: height separates structurally distinct environments, while occupancy density distinguishes sparse from dense scenes. Top- K candidates are retrieved by Euclidean distance in this space, then re-ranked by the full pairwise score (16).

D. Rotation Alignment and Pairwise Scoring

For each retrieved candidate pair, PROBE first resolves the heading ambiguity via FFT-accelerated circular cross-correlation over the max-height grid, then fuses two complementary probabilistic cues into a final similarity score.

1) *FFT-Based Rotation Alignment:* The normalized circular cross-correlation at azimuthal shift δ is

$$\text{CC}[\delta] = \frac{\sum_{r=0}^{R-1} \sum_{s=0}^{S-1} G_m[r, s] G_q[r, (s+\delta) \bmod S]}{\|\mathbf{G}_m\|_F \cdot \|\mathbf{G}_q\|_F}, \quad (10)$$

computed in $\mathcal{O}(R \cdot S + S \log S)$ via the convolution theorem using pre-computed row-wise FFTs. The optimal rotation estimate is

$$\delta^* = \arg \max_{\delta \in \{0, \dots, S-1\}} \text{CC}[\delta]. \quad (11)$$

2) *Bernoulli-KL Jaccard (\mathcal{J}_{KL}):* Classical binary Jaccard treats all cells in the union mask identically, which penalizes boundary mismatches as heavily as interior mismatches. We replace it with a *Bernoulli-KL Jaccard* that models each cell probabilistically and downweights unreliable cells.

Let $\mu_m, \mu_q, \sigma_m, \sigma_q$ denote the Bernoulli mean and uncertainty maps of the map and rotationally-aligned query, respectively. Define the *soft union set* $\mathcal{U} = \{(r, s) : \mu_m[r, s] + \mu_q[r, s] > \epsilon_U\}$ ($\epsilon_U = 10^{-3}$), where the blurred occupancy probabilities μ define the support region rather than the binary mask \mathcal{O} . This ensures that boundary cells whose Gaussian-spread occupancy extends beyond the original footprint participate in the divergence computation, consistent with the continuous marginalization framework.

Step 1: Uncertainty-proportional shrinkage. Rather than using the raw marginal probability μ directly, we shrink each cell’s occupancy toward the uninformative prior $p = 0.5$ in proportion to its Bernoulli uncertainty σ :

$$p_m[r, s] = \mu_m[r, s] \cdot (1 - \sigma_m[r, s]) + 0.5 \cdot \sigma_m[r, s], \quad (12)$$

strictly bounded within $[\epsilon_B, 1 - \epsilon_B]$ for numerical stability ($\epsilon_B = 10^{-6}$). When $\sigma \rightarrow 0$ (confident cell), $p \rightarrow \mu$ and the observation dominates; when $\sigma \rightarrow 0.5$ (maximally uncertain boundary cell), $p \rightarrow 0.5$ and the cell is effectively neutralized, contributing zero KL divergence in subsequent steps.

Step 2: Symmetric KL divergence. For each cell $(r, s) \in \mathcal{U}$, the symmetric KL divergence between the smoothed Bernoulli distributions is

$$D_{KL}[r, s] = \frac{1}{2} (\text{KL}(p_m \| p_q) + \text{KL}(p_q \| p_m)), \quad (13)$$

where $\text{KL}(p \| q) = p \ln(p/q) + (1-p) \ln((1-p)/(1-q))$.

Bernoulli-KL Jaccard. The Bernoulli-KL Jaccard¹ aggregates the per-cell divergence via the arithmetic mean over the soft union \mathcal{U} :

$$\mathcal{J}_{KL}(\delta^*) = \exp\left(-\frac{1}{|\mathcal{U}|} \sum_{(r,s) \in \mathcal{U}} D_{KL}[r, s]\right) \in (0, 1]. \quad (14)$$

Explicit confidence weighting is unnecessary: the shrinkage in Step 1 already drives uncertain cells toward $p=0.5$, where $D_{KL} \rightarrow 0$, so they contribute negligible divergence.

Analysis. When both scans agree ($p_m = p_q$), $D_{KL} = 0$ and $\mathcal{J}_{KL} = 1$. When they disagree, the shrinkage attenuates unreliable cells: Bayesian shrinkage (Step 1) drives uncertain occupancies toward the prior, reducing their KL contribution to near zero. Stable interior mismatches, where both σ values are near zero, dominate the mean KL, producing low \mathcal{J}_{KL} and correct rejection.

3) *Cosine Similarity (\mathcal{C}):* The cosine similarity at the aligned rotation δ^* is

$$\mathcal{C}(\delta^*) = \text{CC}[\delta^*], \quad (15)$$

i.e., the normalized cross-correlation value at the estimated rotation offset (11).

4) *Final Distance: Log-Linear Evidence Fusion:* The PROBE similarity combines two complementary cues:

$$S_{\text{PROBE}} = \mathcal{J}_{KL}(\delta^*) \cdot \mathcal{C}(\delta^*), \quad (16)$$

with distance $d(m, q) = 1 - S_{\text{PROBE}}$.

¹We retain the term ‘‘Jaccard’’ because, like the binary Jaccard index, \mathcal{J}_{KL} is defined over the union of occupied cells and returns 1 for identical inputs.

TABLE II: PROBE Hyper-Parameters (Fixed Across All Experiments)

Symbol	Description	Value
R	Number of distance rings	40
S	Number of azimuth sectors	60
R_{max}	Maximum range [m]	80
σ_t	Translation uncertainty [m]	2.0
ϵ_B	Bernoulli clamp	10^{-6}
v	Voxel grid size [m]	0.5

Probabilistic interpretation. Defining $\ell_1 = \log \mathcal{J}_{KL}$ and $\ell_2 = \log \mathcal{C}$ as log-likelihood contributions from occupancy and height evidence respectively, the multiplicative score becomes

$$\log S_{\text{PROBE}} = \ell_1 + \ell_2, \quad (17)$$

which is a *log-linear model* [17] that aggregates conditionally independent evidence sources. Under the assumption that occupancy agreement and height correlation are independent conditioned on the event ‘‘same place,’’ the product form yields the joint likelihood $P(\text{data} \mid \text{same place}) \propto \mathcal{J}_{KL} \cdot \mathcal{C}$. The multiplicative structure ensures that *both* cues must agree for a high score: a single sufficiently negative cue (low \mathcal{J}_{KL} or low \mathcal{C}) suffices for rejection, consistent with the veto property of likelihood-based fusion.

E. Computational Complexity

Table I compares the key computational costs for descriptor construction and pairwise matching across handcrafted LiDAR descriptors.

Descriptor construction. All compared methods share the same grid-building cost $\mathcal{O}(N)$ for N input points. SC requires no additional processing once the grid is built. Conversely, SC++ creates K' laterally shifted copies of the grid to natively support translation invariance, increasing the construction cost to $\mathcal{O}(K' \cdot N)$. SOLiD incurs an additional $\mathcal{O}(R \cdot H)$ cost for the range-elevation histogram projection with H height bins. PROBE adds an FFT over the azimuthal axis per ring ($\mathcal{O}(R \cdot S \log S)$) and a Jacobian-derived separable Gaussian blur ($\mathcal{O}(R \cdot S)$); both are negligible compared to the point-cloud pass.

Pairwise matching. Here the methods differ substantially. SC aligns two descriptors by exhaustively shifting columns and computing cosine distance at each shift, yielding $\mathcal{O}(K \cdot R \cdot S)$ where K is the search window ($K \leq S$). With SC’s default $S=60$ and a 10% search ratio, each comparison evaluates 6 column shifts (0.1×60). SOLiD reduces matching to a single cosine distance between compact vectors ($\mathcal{O}(R)$), making it the fastest at the pairwise level. PROBE resolves rotation via FFT cross-correlation in $\mathcal{O}(R \cdot S + S \log S)$ using the pre-computed spectra, followed by Bernoulli-KL Jaccard and cosine computation at the aligned rotation in $\mathcal{O}(R \cdot S)$. While the per-pair cost is higher than SOLiD’s vector distance, the FFT-based alignment avoids the linear scan over all column shifts, yielding a log-factor improvement over SC.

TABLE III: Single-Session Place Recognition (AUC, Online Mode, $d_{gt}=10$ m). V-64/32/16: Velodyne HDL-64/32/16; O-128: Ouster OS2-128; CU: ComplexUrban. Best in **bold**, second-best underlined. †: supervised (trained on KITTI).

Method	KITTI (V-64)				HeLiPR (O-128)				NCLT (V-32)				CU (V-16)				Avg
	00	02	05	08	k05	k06	r05	r06	0526	0820	0928	0405	00	01	02	04	
M2DP [13]	.889	.731	.710	.005	.525	.015	.846	.801	.356	.077	.224	.193	<u>.151</u>	.672	.218	.550	.435
SC [2]	.901	.681	.738	.644	.887	.923	.830	.648	.677	.524	.607	.605	.045	.388	.335	.476	.619
LiDAR-Iris [4]	.879	.764	.726	.614	.885	.918	.876	.624	.725	.518	.606	.648	.037	.306	.352	.422	.619
SC++ [3]	.905	.830	.760	.785	<u>.957</u>	<u>.982</u>	.882	.819	.761	.628	.692	.719	.120	.619	.354	.504	.707
RING++ [5]	.826	.755	.859	.704	.911	.933	.981	.968	.776	.686	.625	.660	.818	.905	.296	.815	.782
SOLiD [6]	.892	.674	.710	.752	.706	.618	.734	.563	.492	.344	.491	.591	.008	.136	.142	.265	.507
BEVPlace++† [15]	<u>.911</u>	.901	<u>.775</u>	.948	.983	.989	.854	<u>.845</u>	<u>.847</u>	<u>.758</u>	.815	<u>.798</u>	.058	.526	<u>.377</u>	.568	<u>.747</u>
PROBE (Ours)	.912	<u>.782</u>	.754	<u>.794</u>	.951	.958	<u>.901</u>	.761	.882	.776	<u>.776</u>	.817	.123	<u>.712</u>	.390	<u>.616</u>	<u>.744</u>

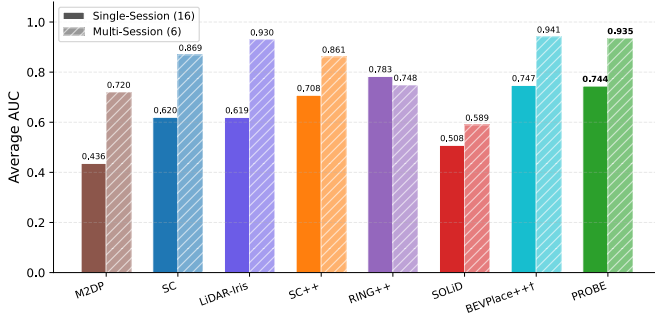


Fig. 4: Average AUC over all single- and multi-session sequence pairs. Solid bars: single-session (16 sequences); hatched bars: multi-session (6 pairs).

IV. EXPERIMENTS

A. Setup

Datasets. We evaluate on four datasets spanning four LiDAR types: **KITTI** [18] (Velodyne HDL-64E, sequences 00/02/05/08), **HeLiPR** [19] (Ouster OS2-128, urban and suburban), **NCLT** [20] (Velodyne HDL-32E, four campus sessions), and **ComplexUrban** [21] (Velodyne VLP-16, dense urban). In total, we report 16 single-session and 6 multi-session sequence pairs (22 configurations).

Evaluation. Single-session matching uses *online* mode: each query retrieves from past frames with a 25 m trajectory-distance exclusion zone. Multi-session uses the full database. Ground-truth positives are pairs within 10 m for all datasets (twice the 5 m database sampling interval).

Baselines. M2DP [13], Scan Context (SC) [2], LiDAR-Iris [4], SC++ [3], RING++ [5], SOLiD [6], and BEVPlace++ [15] (supervised†; trained on KITTI).

Metrics. Precision-Recall (PR) curves, AUC (area under the PR curve), $R@1$ (recall at rank 1), and $F1_{max}$ (maximum F1 score). Tables report AUC; $R@1$ and $F1_{max}$ follow consistent trends and are omitted for conciseness.

Parameters. PROBE uses fixed hyper-parameters across all experiments (Table II).

B. Single-Session Results

Fig. 4 summarizes the average AUC across all single- and multi-session configurations. Table III reports the AUC for

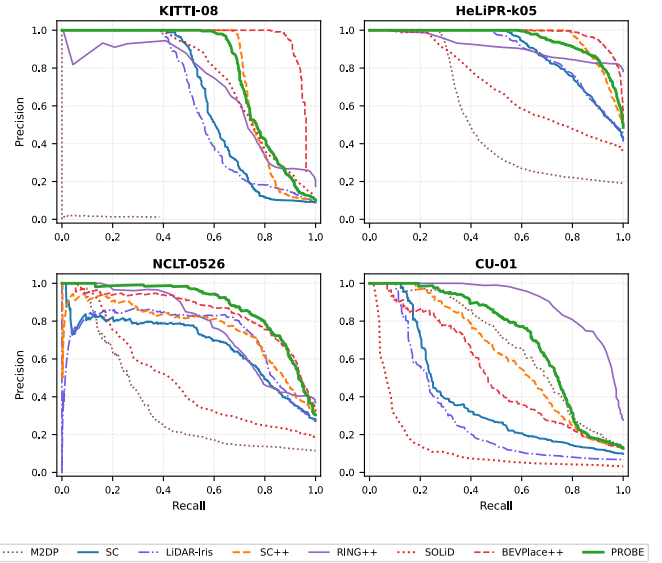


Fig. 5: Single-session Precision-Recall curves (one representative sequence per dataset).

16 single-session sequences across four diverse sensor configurations (Fig. 5 shows representative PR curves). Overall, RING++ achieves the highest average AUC, followed closely by BEVPlace++ and PROBE. PROBE ranks third on average, competitive on 32–128 beam sensors but limited on the sparse 16-beam configuration.

KITTI (V-64). On the dense 64-beam KITTI dataset, the supervised BEVPlace++ yields the highest dataset average, benefiting from being trained directly on this domain. Among the handcrafted methods, PROBE achieves competitive results, leading on seq. 00. PROBE’s continuous formulation does not sacrifice discriminability even in dense environments where binary occupancy is inherently stable.

HeLiPR (O-128). The HeLiPR dataset features the ultra-dense Ouster OS2-128 sensor. Here, RING++ achieves the strongest performance on the riverside sequences, using its translation-invariant Radon-Fourier features that excel under dense spatial sampling. Conversely, BEVPlace++ leads the KAIST sequences. PROBE maintains competitive performance throughout, confirming that the probabilistic blur does not degrade discriminability on high-density grids.

NCLT (V-32). PROBE achieves the highest dataset average on

TABLE IV: Multi-Session Place Recognition (AUC, $d_{\text{gt}}=10\text{m}$). 6 cross-session pairs across two datasets. Best in **bold**, second-best underlined. †: supervised (trained on KITTI).

Method	HeLiPR (O-128)			NCLT (V-32)			Avg
	$k5 \rightarrow 6$	$r5 \rightarrow 6$	$r6 \rightarrow 5$	$26 \rightarrow 20$	$26 \rightarrow 28$	$26 \rightarrow 05$	
M2DP [13]	.869	.824	.806	.808	.797	.214	.720
SC [2]	.983	.861	.876	.927	.914	.648	.868
LiDAR-Iris [4]	.993	.931	.963	.932	.942	<u>.815</u>	.929
SC++ [3]	.980	.860	.862	.931	.926	.603	.860
RING++ [5]	.837	.827	.934	.822	.779	.291	.748
SOLiD [6]	.683	.551	.578	.788	.705	.228	.589
BEVPlace++† [15]	.973	.945	.920	.981	.977	.851	.941
PROBE (Ours)	<u>.986</u>	<u>.941</u>	<u>.940</u>	<u>.979</u>	.977	.785	<u>.935</u>

the 32-beam NCLT dataset, outperforming all baselines including the supervised BEVPlace++, for which NCLT constitutes an unseen domain. These results indicate that the Jacobian-derived σ -gating is effective on sensors possessing sufficient angular density for statistical modeling, yet sparse enough that boundary cells suffer from thresholding artifacts under binary occupancy.

ComplexUrban (V-16). The VLP-16 sensor produces inherently sparse and fragmented BEV grids, posing a significant challenge for geometry-based descriptors. RING++ maintains robust performance due to the global integration properties of the Radon transform. All direct BEV matching methods, including the supervised BEVPlace++ and PROBE, exhibit limited performance on this dataset. Under such extreme sparsity, the continuous KL divergence estimates become noisy, as too few cells are occupied to form a reliable occupancy distribution.

C. Multi-Session Results

Table IV reports AUC for 6 multi-session pairs across HeLiPR and NCLT; Fig. 6 shows representative PR curves. Multi-session evaluation is more challenging due to spatiotemporal variations and differing traversal trajectories.

The supervised BEVPlace++ achieves the highest average AUC. PROBE follows closely, achieving the best results among handcrafted methods and outperforming LiDAR-Iris. RING++, which dominates single-session evaluation, ranks sixth in the multi-session average. While Radon-Fourier features provide translation invariance for locally dense revisits, they lose discriminability when global map and query trajectories diverge across sessions.

HeLiPR. LiDAR-Iris achieves the highest scores on specific sequences. PROBE, however, demonstrates the most consistent robustness, ranking second across all three pairs despite substantial spatiotemporal structural changes.

NCLT. Despite not being trained on NCLT, the learned features of BEVPlace++ generalize effectively, achieving the highest AUCs. PROBE closely follows the supervised baseline, BEVPlace++, matching it on $26 \rightarrow 28$. The analytical σ -gating accommodates the occupancy variations that otherwise degrade binary matching.

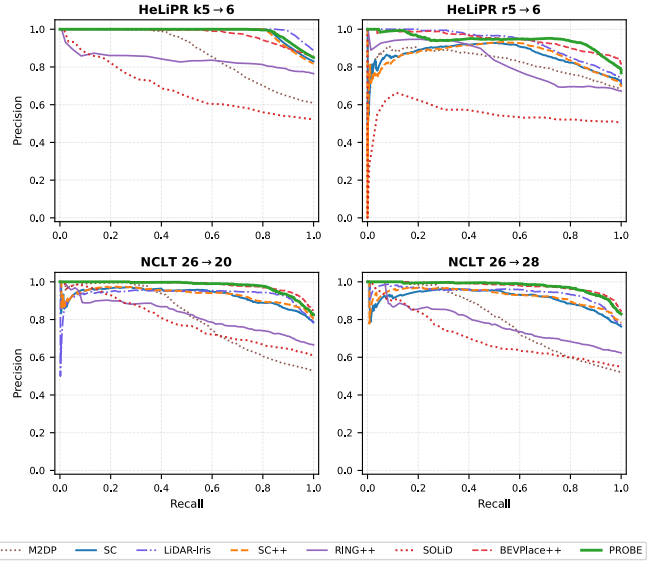


Fig. 6: Multi-session Precision-Recall curves (two representative pairs per dataset, four total).

TABLE V: Ablation Summary (AUC, $d_{\text{gt}}=10\text{m}$). Best in each group in **bold**, second-best underlined.

Group	Variant	Single	Multi
Score	(C1) \mathcal{C} only	<u>.711</u>	<u>.915</u>
	(C2) \mathcal{J}_{KL} only	.691	.902
	(C3) $\mathcal{J}_{KL} \cdot \mathcal{C}$ (ours)	.744	.935
Blur	$\sigma_t = 0$ (binary)	.679	.903
	$\sigma_t = 2\text{m}$ (ours)	.744	.935
	$\sigma_t = 4\text{m}$	<u>.739</u>	<u>.931</u>

D. Ablation Study

We ablate PROBE’s design choices by averaging the AUC across all 16 single-session and 6 multi-session sequence pairs (Table V). All variants construct the identical polar BEV grid, differing only in their scoring formulation and assumed blur strength.

Score components. To isolate each probabilistic matching mechanism, we evaluate variants under fixed uncertainty ($\sigma_t=2\text{m}$): (C1) FFT-aligned cosine \mathcal{C} only, (C2) Bernoulli-KL Jaccard \mathcal{J}_{KL} only, and (C3) Multiplicative fusion $\mathcal{J}_{KL} \cdot \mathcal{C}$ (proposed). The fusion (C3) significantly outperforms individual cues, yielding a $+.033$ (single) and $+.020$ (multi) AUC improvement, validating that probabilistic occupancy agreement and geometric height alignment provide complementary signals.

Blur strength (σ_t). Setting $\sigma_t=0$ completely disables the Jacobian marginalization, reverting the system to deterministic binary matching akin to Scan Context [2]. This binary reduction penalizes the AUC by $.065$ (single-session) and $.032$ (multi-session). Conversely, inflating the uncertainty to $\sigma_t=4\text{m}$ maintains strong multi-session performance but degrades single-session discriminability by $.005$ due to over-smoothing of fine geometric features. We select $\sigma_t=2\text{m}$ as it balances translation tolerance and discriminability.

V. DISCUSSION AND CONCLUSION

We presented PROBE, a probabilistic BEV descriptor that addresses viewpoint sensitivity in LiDAR place recognition. By replacing heuristic binary occupancy with a per-cell Bernoulli model (μ, σ) derived via analytical marginalization over continuous Cartesian shifts, PROBE retains grid-based efficiency while improving cross-session robustness. Density-adaptive scaling prevents over-smoothing on sparse sensors, and multiplicative fusion of the Bernoulli-KL Jaccard and FFT height cosine similarity yields a discriminative, tuning-free pipeline.

Setting $\sigma_t = 0$ collapses PROBE into deterministic binary matching, indicating that the Bernoulli layer is a modular enhancement that reverts to a deterministic baseline.

Performance degrades on low-channel sensors where the BEV grid becomes too sparse for reliable occupancy statistics. Like all BEV descriptors, PROBE also remains vulnerable to extreme translational offsets (> 5 m) that alter observable geometry beyond local marginalization bounds. While currently assuming a 360° FOV, the Bernoulli formulation intrinsically supports restricted-FOV (e.g., solid-state) LiDARs by assigning maximal uncertainty ($\mu=0.5, \sigma=0.5$) to unobserved sectors, safely occluding them via σ -gating. Future work includes explicit radial shift estimation and exploring distributional height encodings to further unify handcrafted geometric foundations with data-driven generalizability.

REFERENCES

- [1] S. Thrun, W. Burgard, and D. Fox, *Probabilistic Robotics*. Cambridge, MA, USA: MIT Press, 2005.
- [2] G. Kim and A. Kim, "Scan context: Egocentric spatial descriptor for place recognition within 3D point cloud map," in *Proc. IEEE/RSJ Int. Conf. Intell. Robots Syst. (IROS)*, 2018, pp. 4802–4809.
- [3] G. Kim, S. Choi, and A. Kim, "Scan context++: Structural place recognition robust to rotation and lateral variations in urban environments," *IEEE Trans. Robot.*, vol. 38, no. 2, pp. 1856–1874, 2022.
- [4] Y. Wang, Z. Sun, C.-Z. Xu, S. E. Sarma, J. Yang, and H. Kong, "LiDAR Iris for loop-closure detection," in *Proc. IEEE/RSJ Int. Conf. Intell. Robots Syst. (IROS)*, 2020, pp. 5769–5775.
- [5] X. Xu, S. Lu, J. Wu, H. Lu, Q. Zhu, Y. Liao, R. Xiong, and Y. Wang, "RING++: Roto-translation-invariant Gram for global localization on a sparse scan map," *IEEE Trans. Robot.*, vol. 39, no. 6, pp. 4616–4635, 2023.
- [6] H. Kim, J. Choi, T. Sim, G. Kim, and Y. Cho, "Narrowing your FOV with SOLiD: Spatially organized and lightweight global descriptor for FOV-constrained LiDAR place recognition," *IEEE Robot. Autom. Lett.*, vol. 9, no. 11, pp. 9645–9652, 2024.
- [7] M. A. Uy and G. H. Lee, "PointNetVLAD: Deep point cloud based retrieval for large-scale place recognition," in *Proc. IEEE Conf. Comput. Vis. Pattern Recognit. (CVPR)*, 2018, pp. 4470–4479.
- [8] X. Chen *et al.*, "OverlapNet: Loop closing for LiDAR-based SLAM," in *Proc. Robot.: Sci. Syst. (RSS)*, 2020.
- [9] J. Ma, J. Zhang, J. Xu, R. Ai, W. Gu, and X. Chen, "OverlapTransformer: An efficient and yaw-angle-invariant transformer network for LiDAR-based place recognition," *IEEE Robot. Autom. Lett.*, vol. 7, no. 3, pp. 6958–6965, 2022.
- [10] J. Komorowski, "MinkLoc3D: Point cloud based large-scale place recognition," in *Proc. IEEE Winter Conf. Appl. Comput. Vis. (WACV)*, 2021, pp. 1790–1799.
- [11] C. Yuan, J. Lin, Z. Liu, H. Wei, X. Hong, and F. Zhang, "BTC: A binary and triangle combined descriptor for 3-D place recognition," *IEEE Trans. Robot.*, vol. 40, pp. 1580–1599, 2024.
- [12] C. Yuan *et al.*, "STD: Stable triangle descriptor for 3D place recognition," in *Proc. IEEE Int. Conf. Robot. Autom. (ICRA)*, 2023.
- [13] L. He, X. Wang, and H. Zhang, "M2DP: A novel 3D point cloud descriptor and its application in loop closure detection," in *Proc. IEEE/RSJ Int. Conf. Intell. Robots Syst. (IROS)*, Daejeon, Korea, 2016, pp. 231–237.
- [14] K. Vidanapathirana, M. Ramezani, P. Moghadam, S. Sridharan, and C. Fookes, "LoGG3D-Net: Locally guided global descriptor learning for 3D place recognition," in *Proc. IEEE Int. Conf. Robot. Autom. (ICRA)*, 2022, pp. 2215–2221.
- [15] L. Luo, S.-Y. Cao, X. Li, J. Xu, R. Ai, Z. Yu, and X. Chen, "BEV-Place++: Fast, Robust, and Lightweight LiDAR Global Localization for Unmanned Ground Vehicles," *IEEE Trans. Robot.*, vol. 41, pp. 4479–4498, 2025.
- [16] Y. Zhang, P. Shi, and J. Li, "LiDAR-based place recognition for autonomous driving: A survey," *ACM Computing Surveys*, vol. 57, no. 4, Art. 106, Dec. 2024.
- [17] C. M. Bishop, *Pattern Recognition and Machine Learning*. New York: Springer, 2006.
- [18] A. Geiger, P. Lenz, and R. Urtasun, "Are we ready for autonomous driving? The KITTI vision benchmark suite," in *Proc. IEEE Conf. Comput. Vis. Pattern Recognit. (CVPR)*, 2012, pp. 3354–3361.
- [19] M. Jung, W. Yang, D. Lee, H. Gil, G. Kim, and A. Kim, "HeLiPR: Heterogeneous LiDAR dataset for inter-LiDAR place recognition under spatiotemporal variations," *Int. J. Robot. Res.*, vol. 43, no. 12, 2024.
- [20] N. Carlevaris-Bianco, A. K. Ushani, and R. M. Eustice, "University of Michigan North Campus long-term vision and lidar dataset," *Int. J. Robot. Res.*, vol. 35, no. 9, pp. 1023–1035, 2016.
- [21] J. Jeong, Y. Cho, Y.-S. Shin, H. Roh, and A. Kim, "Complex urban dataset with multi-level sensors from highly diverse urban environments," *Int. J. Robot. Res.*, vol. 38, no. 6, pp. 642–657, 2019.